Authors Version

Examination of the Oxidation and Metal-Oxide Layer Interface of a Cr-Nb-Ta-V-W High Entropy Alloy at Elevated Temperatures

by

Rebecca Romero[1,2,], Nanthakishore Makeswaran[1,3,*], Ravisankar Naraparaju[3], S.K. Varma[2], C.V. Ramana[1,4]*

[1]Center for Advanced Materials Research, University of Texas at El Paso, 500 West Univ. Ave., El Paso, Texas, 79968

[2]Department of Metallurgical, Materials and Biomedical Engineering, University of Texas, 500 West Univ. Ave.,, El Paso, Texas, 79968

[2]German Aerospace Center (DLR), Institute of Materials Research, Cologne 51170, Germany

[4]Department of Mechanical Engineering, University of Texas, 500 West Univ. Ave.,, El Paso, Texas, 79968

#: Equal contribution from authors.

Journal of Materials Research and Technology 23, (2021), 2100164
https://doi.org/10.1002/ADEM.202100164

Examination of the Oxidation and Metal-Oxide Layer Interface of a Cr-Nb-Ta-V-W High Entropy Alloy at Elevated Temperatures

ABSTRACT

The authors report on the evaluation of the oxidation and the interface microstructure of a Cr-NbTa-V-W refractory high entropy alloy (HEA) at higher temperatures. The bulk metal-oxide layer interface of the Cr-Nb-Ta-V-W HEA was exposed to temperatures of 700 and 800^{o}C in air and examined in the oxidized state. Combined *in-situ* X-ray diffraction coupled with *ex-situ* scanning electron microscopy (SEM) and energy dispersive X-ray spectrometry (EDS) analyses confirm the five different phases which were previously identified in this alloy. The microstructure near the interface was studied for an indication of selective oxidation of this alloy. Oxidized samples at 700 and 800^{o}C were studied to evaluate the differences in oxide composition and morphology at interface and surface layer. SEM was employed to evaluate the physical structure of the interface and oxide surface layer, while EDS and X-ray color mapping was utilized to characterize the elemental composition of the bulk metal and oxide layers. Cracking and porosity were found along the interface layer which grew directionally outward. Two main oxides were identified: a W-based oxide with a needle-like structure and a Cr-Ta oxide with a granular structure that was primarily found in clusters.

Keywords: Refractory High Entropy Alloys; Nb-Cr-V-W-Ta; Oxidation; Microstructure

1. Introduction

As service conditions become more severe and push the limits of what materials can operate in, the demand for innovative materials that can withstand said conditions continues to grow. High temperature applications are showing to be an emerging field in materials systems, specifically in

the power generation and nuclear industries. It has become crucial that component materials bear excellent high temperature properties. A relatively new alloying concept was originally proposed by Yeh et al. [1-4] termed high entropy alloys (HEAs), has shown promising results. The objective was to create a new approach to alloy design, focusing on systems with multiple principal elements in equimolar or near-equimolar ratios rather than one principal element as the matrix. The alloy system is defined as one containing at least five elements in equiatomic proportion. Various reviews are found in literature [5-8].

Many HEAs have demonstrated having exceptional properties, which include excellent strength [9], high corrosion resistance and fracture strength [10], and thermal stability [11] since being proposed. For a BCC-structured $AlCoCrFeNiTi_x$ system, the alloy displayed excellent strength at room temperature [12]. A compressive yield strength of over 3 GPa was achieved, along with excellent plastic strain properties. The ability to achieve impressive mechanical properties prompted further research into elevated temperature studies. A study of a Al0.5CoCrCuFeNi HEA demonstrated the effects of temperature on mechanical properties [13]. The HEA exhibited a decrease in strength and hardness with an increase in temperature. Because high temperature properties are vital for many of these HEAs, this gave rise to the concept of refractory HEAs [14] originally proposed by Senkov et al.

The objective of refractory HEA research is to create a class of materials primarily based on refractory element constituents such as Mo, Ta, W, Nb, and V [14]. The motive for using refractory elements is because of their high melting temperatures, which would be well utilized in high temperature service conditions. Within the past decade, several studies have been done to further investigate many of these HEAs. For example, Senkov et al. [15-16] reported the mechanical properties and microstructures of different refractory HEAs. They found that both the $Nb_{25}Mo_{25}Ta_{25}W_{25}$ and $V_{20}Nb_{20}Mo_{20}Ta_{20}W_{20}$ alloys exhibit good plastic flow with compressive strain. Further CALPHAD simulations were performed on a senary HEA of $Cr_xMoNbTaVW$ composition [17] which found that the calculated enthalpy of mixing increased strongly with an increase in Cr content. This subsequently destabilized the BCC phase that was identified. Several

HEAs have proven to be useful at high temperatures because of their high strength [15-16] and microstructural stability [18] at elevated temperatures, however the oxidation behavior on many of the alloy systems has not been investigated in great detail.

The present work aims to investigate the bulk metal-oxide layer interface of a Cr-Nb-Ta-V-W refractory HEA. The HEA was subjected to in-situ x-ray diffraction at temperatures up to 800^{o}C to determine oxidation patterns. A cross-sectional examination of the interface was conducted to show any indications of selective oxidation and evaluate the microstructure near the interface. The surface layer of the oxide was also analyzed for a full chemical and physical oxide analysis. Thus, as presented and discussed in this paper, combined *in-situ* structural and *ex-situ* microstructure, chemical analyses allowed us to examine, validate and confirm the oxide phases and the alloyoxide interface microstructure.

2. Materials and Methods

2.1. Cr-Nb-Ta-V-W HEAs

Characterization was performed on 5 mm x 5 mm x 5 mm cubes of equiatomic Cr-Nb-TaV-W high entropy alloy. The cubes of Cr-Nb-Ta-V-W HEAs were procured from Plasma Materials Inc. (Livermore, California, USA) and were made by arc melting using metals of at least three nines purity. The as-received samples were cubes which were prepared with 5 mm edges by electrical discharge machining (EDM). Two cubes were supplied in a pre-oxidized state having been heat treated at 700 and 800°C respectively for 24 hours. These samples were subjected to cross sectional SEM and EDS measurements. The third cube was supplied untreated and was subjected to high temperature XRD measurements to determine oxide growth patterns. Two separate samples were also oxidized for 48 hours, one at 700^{o}C and one at 800^{o}C, so that the surface oxide layer could be examined. Samples were oxidized in a Sentrotech furnace with computer-controlled heating and cooling cycles for isothermal heating. A heating rate of 10^{o}C per minute

was utilized up to the selected oxidation temperature. The samples were then cooled to room temperature inside the furnace.

2.2. Metallographic Sample Preparation

Cross sectional analysis of the pre heat-treated samples was facilitated by the use of precision cut-off machines set to a cutting rate of 0.005 mm/s, utilizing an abrasive cutting disk. Before cutting, the samples were stabilized using a two-component epoxy adhesive. The purpose of the adhesive is to fill any open gaps and provide more stability when cutting, grinding, and polishing the sample. Previous attempts to cut the sample without reinforcement led to separation of the oxide from the remaining metal core. The samples, cut through the primary part of the CMAS melt/coating interface, was kept upright via metal clips and hot-embedded in electrically conductive synthetic embedding material (Struers, Polyfast). Embedding was performed at 180°C for 6 minutes while pressure was increased from 50N to 75N after 3 min. Following an additional 6 minutes, the sample was water cooled before removal. completed by with standard metallographic preparation procedures. The samples were polished using a series of diamond discs ranging from 220 grit to 8 µm, followed with an alcoholic diamond suspension, then a Al_2O_3 oxide suspension (Masterprep), before completing a final cleaning with detergent and water for 20 minutes. All polishing was done with an applied pressure of 10 N. A thin platinum layer was applied via sputtering for 30 seconds before beginning SEM analysis to prevent charging effects. For the non-heat-treated sample, preparation was limited to cutting the cube in half using the appropriate cutting procedures.so it would fit within the confines of the XRD sample holder and using a 220 grit polishing disk to even out the sample surface for mounting.

2.3. Scanning Electron Microscopy (SEM) and Energy Dispersive X-Ray Spectroscopy (EDS)

Microstructural analysis of the pre-oxidized samples was undertaken using scanning electron microscopy (DSM Ultra 55, Carl Zeiss NTS) which had been equipped with an energy dispersive X-ray spectroscopy (EDS) system (Inca, Oxford Instruments). The energy selective backscatter (AsB) electron detector was also used to provide topographical clarity. EDS elemental mapping, in conjunction with area and spot analysis of the captured images was done to determine

the chemical composition of the final oxides, transition layer, and remaining metallic structure of the samples.

To observe the oxidized surface layer, scanning electron microscopy was performed with a Hitachi SU 3500 using the backscattered electron and secondary electron mode. The compositions of the oxides were determined by EDS with the use of x-ray color mapping to allow for the determination of elements.

2.4. High Temperature X-Ray Diffraction (XRD)

To understand the oxide evolution of the high entropy alloy at elevated temperatures, the non-oxidized alloy sample was measured in a high temperature XRD system (Bruker). In order to maintaining consistency with previously conducted experiments, and to allow for a direct comparison with the two pre-oxidized samples, the alloy was heated to a maximum temperature of 800°C with a heating rate of 10°/min. Measurements were taken at 100°C intervals starting at 100°C and continuing through 800°C. At each interval the temperature was kept constant for 20 minutes to allow for stabilization before actual measurements commenced for 30 minutes. With final measurements complete the sample was air cooled to room temperature.

3. Results and Discussion

3.1 Cross-Sectional Bulk Metal-Oxide Interface - SEM

The SEM cross-section of the bulk metal-oxide layer interface of the oxidized sample at 700^{o}C can be seen in Figure 1. EDS spot analysis was performed to estimate the composition of different areas. Medium gray areas are visible within the bulk metal that are identified as phase three which consists of Cr rich structure containing a mixture of a Ta-Cr solid solution and a Laves phase VTa_2 previously identified [18]. This is confirmed by EDS is the area marked B. Some cracking and porosity is visible within the phase. A darker grey area is visible within the phase, marked A, is determined to be a Ta-rich oxide and was confirmed with EDS performed. Figure 1 includes the elemental analysis indicating the presence of this Ta-rich oxide. An area marked as C further

confirms the presence of the phase three previously described, which contains a large amount of cracking throughout the structure. The oxide layer itself shows to be non-uniform with evidence of porosity and cracking throughout the layer near the interface. An area marked D is within the oxide layer is a mixture of all of the elements, but mostly of a W and Ta oxide formation. The large, dark pore near the bottom left-hand corner of the image is representative of a VO_x pore [19] identified in an $NbCrMoTiVAl_{0.5}$ alloy. These were found to have most likely formed as a result of fusion or volatilization of a V_2O_5 oxide. A low melting point of V_2O_5 at 670^{o}C [20] is likely to have been a contributing factor to this.

Figure 2 confirms the presence of the phases found in [18] including a W rich phase, a cloudy Nb rich phase in solid solution with V, Cr, and Ta and a Cr phase in solid solution with Ta. Tantalum appears to cluster around chromium rich areas. Both elements appear to stay in solution in the bulk metal and do have a strong presence in the oxide layer, which is evident in the EDS color mapping. Cracking and voids are present at the boundary of the interface which grow upward into the oxide layer and are indicated in Figure 2. Tungsten and V appear the most in the oxide layer, indicating that these are the first to oxidize. Figure 3 illustrates the nonuniformity of the oxide layer, which appears as a thick porous layer. The large pores can be linked to the presence of W and Ta in the oxide layer in areas near each other because of the difference in coefficient of thermal expansion (CTE) [21,22]. When there is a large difference in CTE, one oxide may cool faster, which in this case is W, and causes a difference in contraction leaving a void space. In this case, W has a CTE of approximately $4.8x10^{-6}$, while Ta has a CTE of approximately $6.7x10^{-6}$. Tungsten appears vertically in the oxide layer, indicating an upward directional growth of the oxide layer. This is visible through the EDS color mapping where strings of W appear throughout the layer. Ta clusters around neighboring regions of W in the oxide layer. Clusters of a W-Ta oxide appear above the surface layer and within some of the large pores, which is highlighted in the color mapping. Nb, Cr, and V appear to remain in solution in the bulk metal, with the exception of Cr which appears in small amounts throughout the oxide layer. Figure 4 shows the thickness of the grown oxide layer, which shows large variation along the surface. The thickness ranges from 391.2 μm to 461.1 μm. This thickness measurement less than measured of the alloy CrMoNbTaV, which

ranged from 530 μm to 1132 μm, though these measurements were taken at temperatures in the range of 900°C to 1100°C [23].

The cross-section of the interface of the oxidized sample at 800°C is shown in Figure 5. A significant amount of porosity and separation appears at the interface which was similar to what was seen at 700°C, possibly due to the occurrence of spallation. The porosity is once again believed to be a result of a V-oxide which melted or the difference in CTE. No single element appears to predominate in the oxide layer, though there are areas of a Cr-rich and W-rich oxide dispersed throughout. Figure 6 shows a similar oxide layer to that at 700°C, which is non-uniform and porous in nature. V appears in small clusters, closer to the interface area. Very little V is seen near the surface of the oxide layer. W again shows a linear, directional upward growth from the interface. Cr appears in clusters spread relatively evenly throughout the oxide layer. Nb and Ta do not appear heavily throughout the oxide layer, however Ta remains in the bulk metal right below the interface. Figure 7 shows the thickness of the oxide layer, which is relatively even. The thickness was measured in the range from 1.313 mm to 1.379 mm which is comparable to the results found in [23].

3.2 Surface Analysis - SEM

Additional surface analysis of the oxide layers was performed to examine the morphology and chemical composition of the oxides which were grown at 700°C and 800°C 48 hours in order to compare with the cross-section analysis. At both temperatures, the oxides show a similar physical morphology, however the oxide layer is more dense at the 800°C sample.

Figure 8 shows the top surface of the 700°C sample. Evidently, a very porous oxide, spread throughout the surface can be seen. There are two prominent oxides present, one of a Ta-Cr oxide with some trace amounts of Nb. The oxide has a granular structure which surround a large pore. Extending out of the oxides are the beginnings of W-oxide whiskers. The other main oxide present are thin, W-oxide whiskers which grow outwards and appear as the lighter structures in the image. This is the most prominent oxide present on the top surface of the oxide layer.

The 800°C sample can be seen in Figure 9. The structure is very similar to that of the 700°C sample, however the oxides are more dense and there is less porosity. The most prominent oxide present is once again a W-oxide. They are once again whisker-like, but longer than what was seen on the previous sample. This is indicative that the oxides grow in size with an increase in temperature. The granular Ta-Cr oxide is once again present, but shows indications of the whiskerlike oxides growing out of them. Both of the images utilized EDS to confirm the chemical compositions of the oxides. These results may shed some light on the effectiveness of refractory metals in the HEA composition towards surface as well as interface oxidation of the alloy. Although the oxidation rates of pure refractory metals, W, Ta and Nb, are very high at much higher temperatures than those employed in this work, the observed trends and differences at 700-800°C in these HEAs can be still accountable to their respective oxide formation or growth mechanisms. Undoubtedly, as evident in SEM and EDS analyses, all of the metals in the HEA oxidize and form their respective solid oxides. However, the outward growth of W-oxide, which also is the most prominent oxide present on the top surface of the oxide layer as indicated by the SEM and EDS analyses, may be due to higher oxidation rate of W compared to Nb and Ta. Such contrast was also noted in the high-temperature oxidation behavior of a family of refractory high-entropy alloys (HEAs) with compositions of W–Mo–Cr–Ti–Al, Nb–Mo–Cr–Ti–Al and Ta–Mo–Cr–Ti–Al [24].

3.3 Oxide Growth - High Temperature XRD

In-situ high temperature XRD was performed on an unoxidized sample with 100°C increments up to 800°C to understand the oxide growth with increasing temperature. Figure 10 shows the XRD data stacked vertically in terms of varying temperature. At 100°C, there are little to no indications of oxide growth. The main peaks identified are of metal compounds, with the exception of Cr, which did not appear as a peak for any compounds. This continues as the temperature increases up till 500°C. There are small peaks of different V-oxides, indicating that V is the first element to oxidize. The peaks of V-oxides change from V_3O_7 and $V_{14}O_6$ to VO_2 at 600°C, indicating that more oxygen is introduced into the system at higher temperatures. There is no indication of any proven type of protective oxides previously identified [25] including $CrTaO_4$ and Cr_2O_3. At 700°C

peaks of NbO_2 and WO_3 appear, for which they are then identified again at 800°C. Nb_2O_5 peaks also appear at this temperature, though this was not found in the cross section of the sample. None of the identified peaks are considered protective oxides, indicating that oxygen is able to diffuse into the material faster and explains for the more dense oxide layer at higher temperatures.

The SEM and EDS analysis performed in conjunction with the in-situ analysis provided further insight how this material oxidizes, and the oxide layer forms. The XRD results picked up V oxide peaks forming at lower temperatures; however this did not appear in the cross-sectional or oxide surface layers. This is most likely due to the low melting point of V oxides that create porous structures. Because the sample was only held at temperature for 20 minutes during the in-situ XRD, this most likely did not allow enough time for the oxide to melt and allowed for the detection of the V oxides, but when held for longer periods, the oxide was able to melt and was not detected in the image analysis but rather left large pores throughout the structure. Tungsten appeared throughout the oxide layer and at the surface at both 700°C and 800°C, which explains for the detection of WO_3. This is the elongated, whisker-like oxide found at the surface and vertically throughout the cross-sectional layer.

4. Conclusions

The oxide layer-bulk metal interface of a high entropy alloy was examined to further understand if there is any selective oxidation which occurs, the way in which oxides grow outward from the metal, and to characterize the morphology and compositions of the surface layer of the oxide layer. The key findings in this study are summarized as following:

1. No specific indications of selective oxidation was found along the interface, though there is some Ta-oxide that agglomerates near the interface. A significant amount of cracking and porosity was also found along the interface. Previous microstructures of this alloy compositions were confirmed, including the five phases previously indicated.

2. Many of the oxides cluster within the oxide layer. The only exception to this is W, which grows outward vertically within the layer. No protective oxides were found, which explains the dense structure of the oxide layer at a higher temperature.
3. A Cr-Ta oxide of a granular morphology. There were trace amounts of Nb found within the oxide. A W- oxide was also found, as a long, whisker-like morphology. This was thought to be WO_3 based on the XRD results.

Acknowledgements

This work/manuscript is a contribution from the Center for Advanced Materials Research (CMR). The authors acknowledge, with pleasure, support from the National Science Foundation with NSF-PREM grant #DMR-1827745.

5. References

1. Yeh, J. W., Chen, S. K., Lin, S. J., Gan, J. Y., Chin, T. S., Shun, T. T., Tsau, C. H., & Chang, S. Y. (2004). Nanostructured high-entropy alloys with multiple principal elements: Novel alloy design concepts and outcomes. Advanced Engineering Materials, 6(5), 299–303. https://doi.org/10.1002/adem.200300567
2. Yeh, J., Chen, S., Gan, J., Lin, S., & Chin, T. (2010). Communications: Formation of Simple Crystal Structures in Cu-Co-Ni-Cr-Al-Fe-Ti-V Alloys with Multiprincipal Metallic Elements. 35(August 2004), 2533–2536.
3. Tong, C. J., Chen, Y. L., Chen, S. K., Yeh, J. W., Shun, T. T., Tsau, C. H., Lin, S. J., & Chang, S. Y. (2005). Microstructure characterization of AlxCoCrCuFeNi high-entropy alloy system with multiprincipal elements. Metallurgical and Materials Transactions A: Physical Metallurgy and Materials Science, 36(4), 881–893. https://doi.org/10.1007/s11661-005-0283-0
4. Yeh, J. W., Chang, S. Y., Hong, Y. Der, Chen, S. K., & Lin, S. J. (2007). Anomalous decrease in X-ray diffraction intensities of Cu-Ni-Al-Co-Cr-Fe-Si alloy systems with multi-principal elements. Materials Chemistry and Physics, 103(1), 41–46.

https://doi.org/10.1016/j.matchemphys.2007.01.003

5. Chen, J., Zhou, X., Wang, W., Liu, B., Lv, Y., Yang, W., Xu, D., & Liu, Y. (2018). A review on fundamental of high entropy alloys with promising high–temperature properties. Journal of Alloys and Compounds, 760, 15–30. https://doi.org/10.1016/j.jallcom.2018.05.067
6. Miracle, D. B., & Senkov, O. N. (2017). A critical review of high entropy alloys and related concepts. *Acta Materialia*, *122*, 448–511. https://doi.org/10.1016/j.actamat.2016.08.081
7. Williams, T. I. (1988). Science and technology in Eastern Europe. *Endeavour*, *12*(4), 193. https://doi.org/10.1016/0160-9327(88)90170-6
8. Tsai, M. H., & Yeh, J. W. (2014). High-entropy alloys: A critical review. *Materials Research Letters*, *2*(3), 107–123. https://doi.org/10.1080/21663831.2014.912690
9. Juan, C. C., Tsai, M. H., Tsai, C. W., Lin, C. M., Wang, W. R., Yang, C. C., Chen, S. K., Lin, S. J., & Yeh, J. W. (2015). Enhanced mechanical properties of HfMoTaTiZr and HfMoNbTaTiZr refractory high-entropy alloys. *Intermetallics*, *62*, 76–83. https://doi.org/10.1016/j.intermet.2015.03.013
10. Xiao, D. H., Zhou, P. F., Wu, W. Q., Diao, H. Y., Gao, M. C., Song, M., & Liaw, P. K. (2017). Microstructure, mechanical and corrosion behaviors of AlCoCuFeNi-(Cr,Ti) high entropy alloys. *Materials and Design*, *116*, 438–447. https://doi.org/10.1016/j.matdes.2016.12.036
11. Yao, H. W., Qiao, J. W., Gao, M. C., Hawk, J. A., Ma, S. G., Zhou, H. F., & Zhang, Y. (2016). NbTaV-(Ti,W) refractory high-entropy alloys: Experiments and modeling. *Materials Science and Engineering A*, *674*, 203–211. https://doi.org/10.1016/j.msea.2016.07.102
12. Zhou, Y. J., Zhang, Y., Wang, Y. L., & Chen, G. L. (2007). Solid solution alloys of AlCoCrFeNi Tix with excellent room-temperature mechanical properties. *Applied Physics Letters*, *90*(18). https://doi.org/10.1063/1.2734517

13. Tsai, C. W., Tsai, M. H., Yeh, J. W., & Yang, C. C. (2010). Effect of temperature on mechanical properties of Al0.5CoCrCuFeNi wrought alloy. *Journal of Alloys and Compounds*, *490*(1–2), 160–165. https://doi.org/10.1016/j.jallcom.2009.10.088
14. Senkov, O. N., Wilks, G. B., Miracle, D. B., Chuang, C. P., & Liaw, P. K. (2010). Refractory high-entropy alloys. *Intermetallics*, *18*(9), 1758–1765. https://doi.org/10.1016/j.intermet.2010.05.014
15. Senkov, O. N., Wilks, G. B., Scott, J. M., & Miracle, D. B. (2011). Mechanical properties of Nb25Mo25Ta 25W25 and V20Nb20Mo 20Ta20W20 refractory high entropy alloys. *Intermetallics*, *19*(5), 698–706. https://doi.org/10.1016/j.intermet.2011.01.004
16. Senkov, O. N., & Woodward, C. F. (2011). Microstructure and properties of a refractory NbCrMo0.5Ta0.5TiZr alloy. *Materials Science and Engineering A*, *529*(1), 311–320. https://doi.org/10.1016/j.msea.2011.09.033
17. Zhang, B., Gao, M. C., Zhang, Y., & Guo, S. M. (2015). Senary refractory high-entropy alloy CrxMoNbTaVW. *Calphad: Computer Coupling of Phase Diagrams and Thermochemistry*, *51*, 193–201. https://doi.org/10.1016/j.calphad.2015.09.007
18. Varma, S. K., Sanchez, F., & Ramana, C. V. (2020). Microstructures in a Nb-Cr-V-W-Ta high entropy alloy during annealing. *Journal of Materials Science and Technology*, *53*, 66–72. https://doi.org/10.1016/j.jmst.2020.03.028
19. Liu, C. M., Wang, H. M., Zhang, S. Q., Tang, H. B., & Zhang, A. L. (2014). Microstructure and oxidation behavior of new refractory high entropy alloys. *Journal of Alloys and Compounds*, *583*, 162–169. https://doi.org/10.1016/j.jallcom.2013.08.102
20. Speight, J.G. Lange's Handbook of Chemistry. 16th edition, Laramie: CD&W, Inc. ; 2005
21. Hidnert, P. (1929). Thermal expansion of tantalum. Bureau of Standards Journal of Research, 2(5), 887. https://doi.org/10.6028/jres.002.028
22. Hidnert, P., & Sweeney, W. T. (1925). Thermal expansion of tungsten. Scientific Papers of the Bureau of Standards, 20, 483. https://doi.org/10.6028/nbsscipaper.203
23. Xiao, Y., Kuang, W., Xu, Y., Wu, L., Gong, W., Qian, J., Zhang, Q., & He, Y. (2019).

Microstructure and oxidation behavior of the CrMoNbTaV high-entropy alloy. Journal of Materials Research, 34(2), 301–308. https://doi.org/10.1557/jmr.2018.340

24. Gorr, B., Muller, F.; Azim, M.; Christ, H.-J., Muller, T., Chen, H., Kauffmann, A., Heilmaier, M. (2017). High-temperature oxidation behavior of refractory high-entropy alloys: effect of alloy composition. Oxidation of Metals, 88, 339-349. https://doi.org/10.1007/s11085-016-9696-y
25. Lo, K. C., Chang, Y. J., Murakami, H., Yeh, J. W., & Yeh, A. C. (2019). An oxidation resistant refractory high entropy alloy protected by CrTaO4 -based oxide. *Scientific Reports*, *9*(1), 3–4. https://doi.org/10.1038/s41598-019-43819-x

Figure Captions

Figure 1: SEM cross section of bulk metal-oxide interface of the oxidized sample at 700^{o}C in SE mode. The boundary line between the bulk metal and oxide layer is indicated by the red arrow. Cracking and porosity is visible just below and within the oxide interface. Local EDS analysis was also performed in four areas noted on the figure. The atomic percentage of each element is outlined in the corresponding table.

Figure 2: Bulk metal-oxide interface of the oxidized sample at 700^{o}C in BSE mode with EDS color mapping. Various phases appear in solution within the bulk metal, while W and V are the main constituents which appear in the oxide layer. Voids at the boundary layer that grow into the oxide layer are indicated in the figure.

Figure 3: Bulk metal-oxide interface of the oxidized sample at 700^{o}C in the BSE mode with corresponding EDS color mapping. Significant amounts of porosity are visible within the oxide layer. Lighter W oxides are present in the oxide layer as the lighter vertical areas in the layer with

small clusters of Ta in neighboring regions. An area of W-Ta clusters appear above the surface of the oxide layer and in regions between the voids.

Figure 4: Bulk metal-oxide interface of the oxidized sample at 700^{o}C in the BSE mode indicating the thickness of the oxide layer.

Figure 5: Bulk metal-oxide interface of the oxidized sample at 800^{o}C in the SE mode with large, prominent pores just above the interface.

Figure 6: Bulk metal-oxide interface of the oxidized sample at 800^{o}C in the BSE mode with EDS color mapping. Large, porous areas are visible throughout the oxide layer. Clusters of Cr are dispersed throughout the oxide layer. Strings of W with vertical upward growth in the layer are also dispersed throughout the oxide layer.

Figure 7: Bulk metal-oxide interface of the oxidized sample at 800^{o}C in the BSE mode indicating the thickness of the oxide layer.

Figure 8: Surface of the oxide layer at 700^{o}C in the BSE mode. The two main oxides are visible, the granular Cr-Ta oxide and the whisker-like W oxide.

Figure 9: Surface of the oxide layer of the 800^{o}C sample in the BSE mode. The granules of the Cr-Ta oxide have become more defined, while the W oxide has become more needle-like and is more prominent.

Figure 10: In-situ x-ray diffraction data of the HEAs.

Figure List:

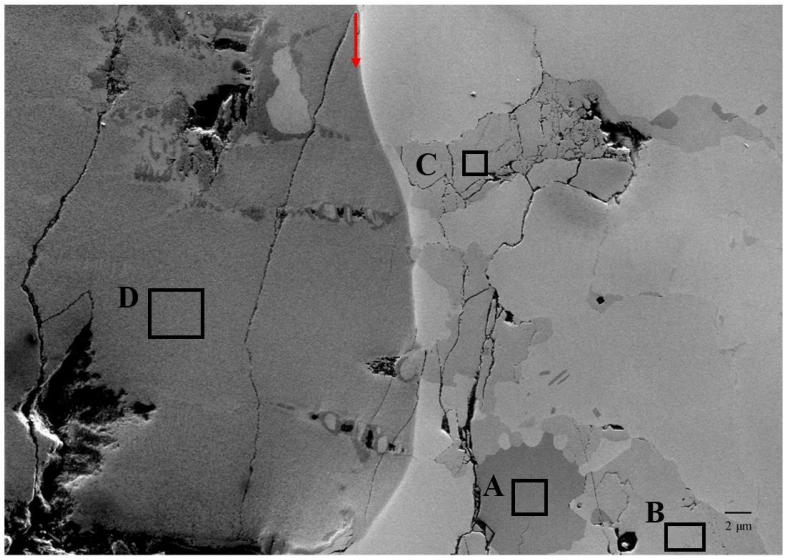

	A	B	C	D
O	62.13	3.08	5.99	63.73
V	11.71	11.00	12.42	7.66
Cr	0.71	45.14	42.27	4.21
Nb	0.89	9.27	5.04	3.38
Ta	23.46	24.39	26.44	10.10
W	1.11	7.13	7.83	10.92
Total	100.0	100.0	100.0	100.0

Figure 5: SEM cross section of bulk metal-oxide interface of the oxidized sample at 700^{o}C in SE mode. The boundary line between the bulk metal and oxide layer is indicated by the red arrow. Cracking and porosity is visible just below and within the oxide interface. Local EDS analysis was also performed in four areas noted on the figure. The atomic percentage of each element is outlined in the corresponding table.

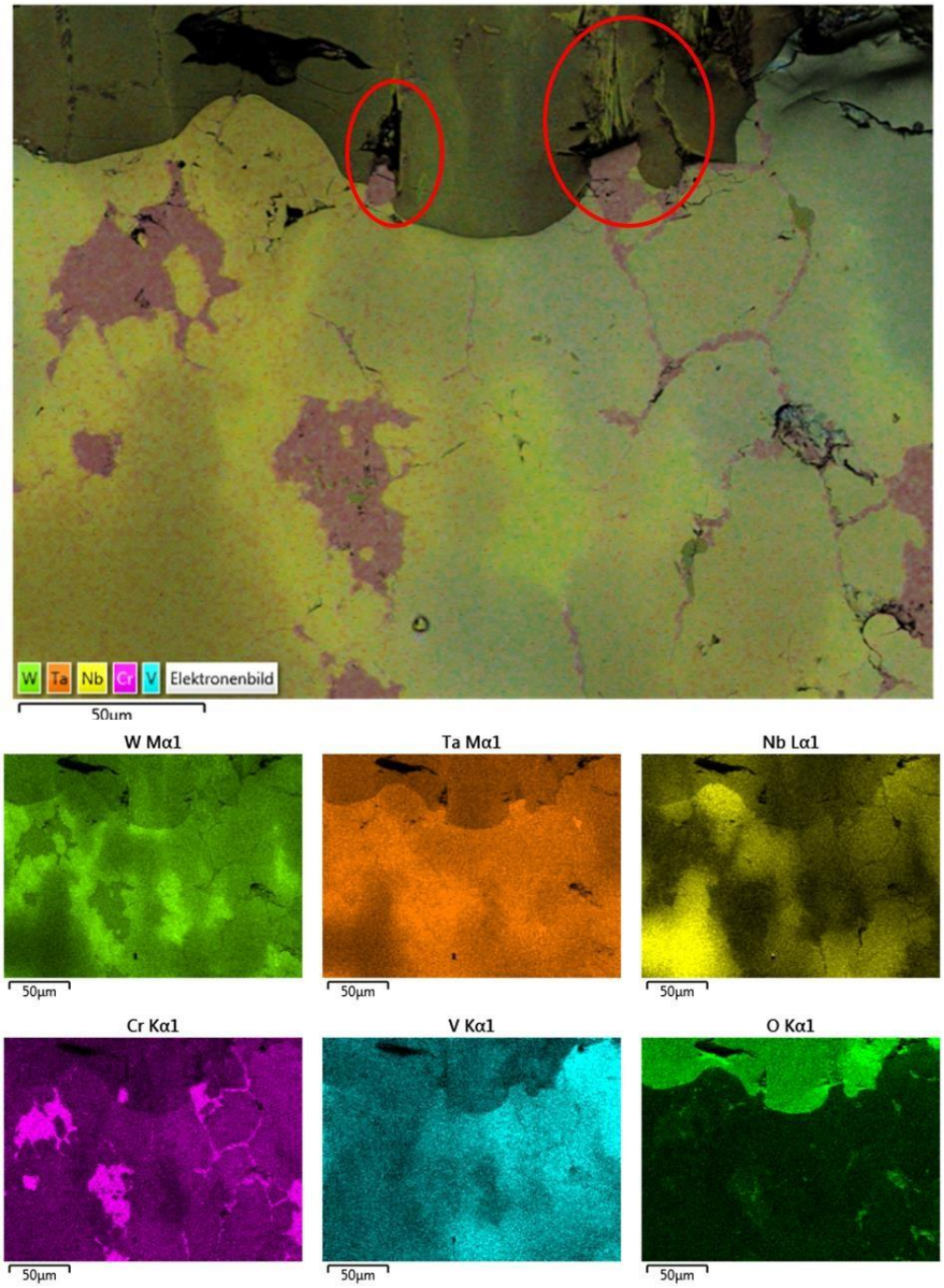

Figure 6: Bulk metal-oxide interface of the oxidized sample at 700°C in BSE mode with EDS color mapping. Various phases appear in solution within the bulk metal, while W and V are the main constituents which appear in the oxide layer. Voids at the boundary layer that grow into the oxide layer are indicated in the figure.

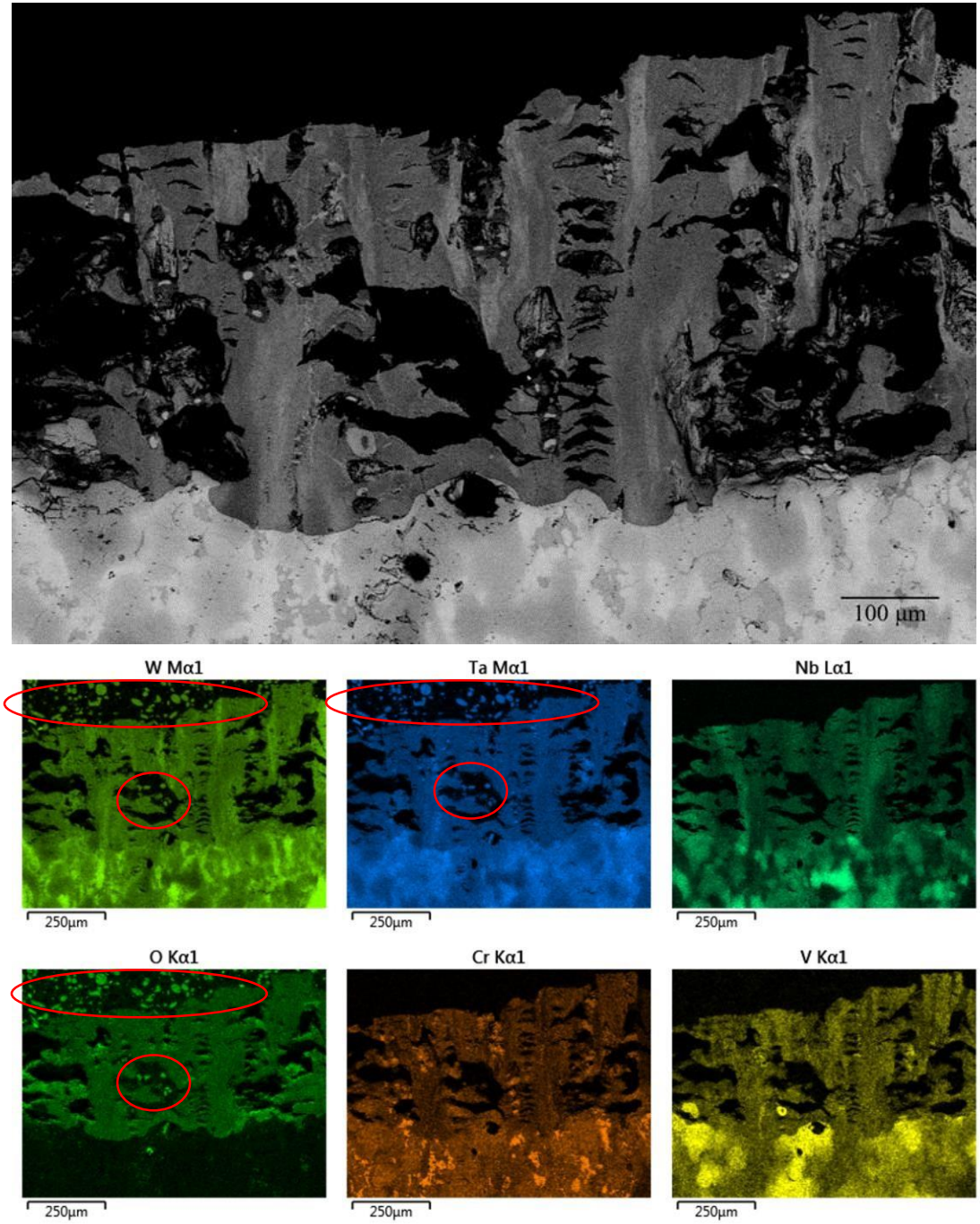

Figure 7: Bulk metal-oxide interface of the oxidized sample at 700°C in the BSE mode with corresponding EDS color mapping. Significant amounts of porosity are visible within the oxide layer. Lighter W oxides are present in the oxide layer as the lighter vertical areas in the layer with small clusters of Ta in neighboring regions. An area of W-Ta clusters appear above the surface of the oxide layer and in regions between the voids.

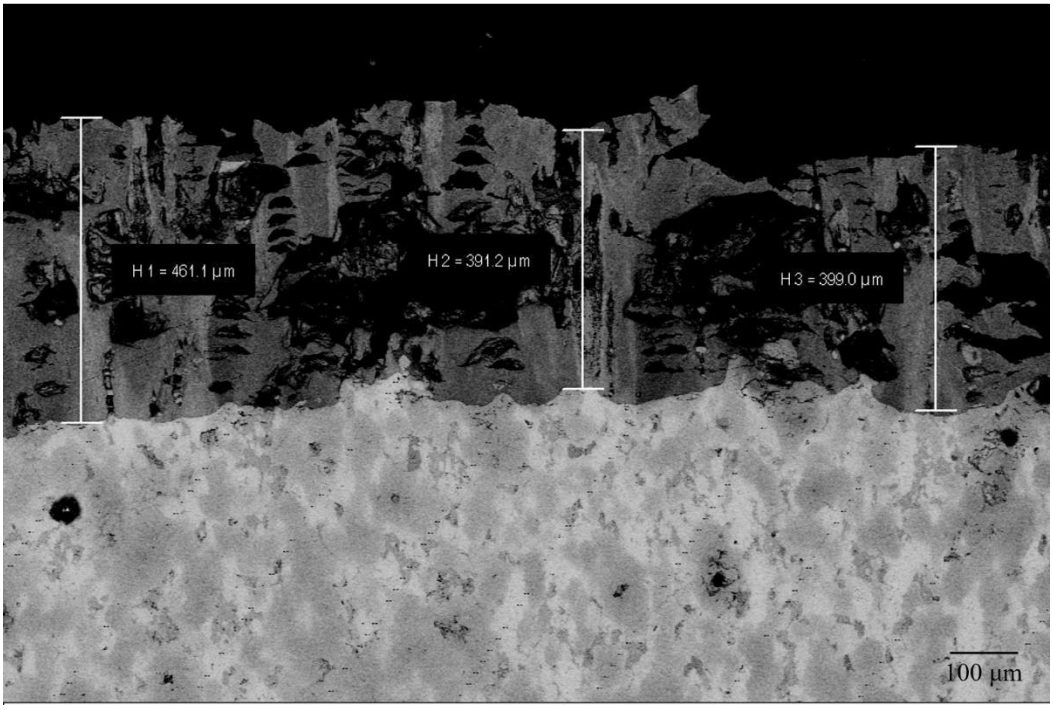

Figure 8: Bulk metal-oxide interface of the oxidized sample at 700^{o}C in the BSE mode indicating the thickness of the oxide layer.

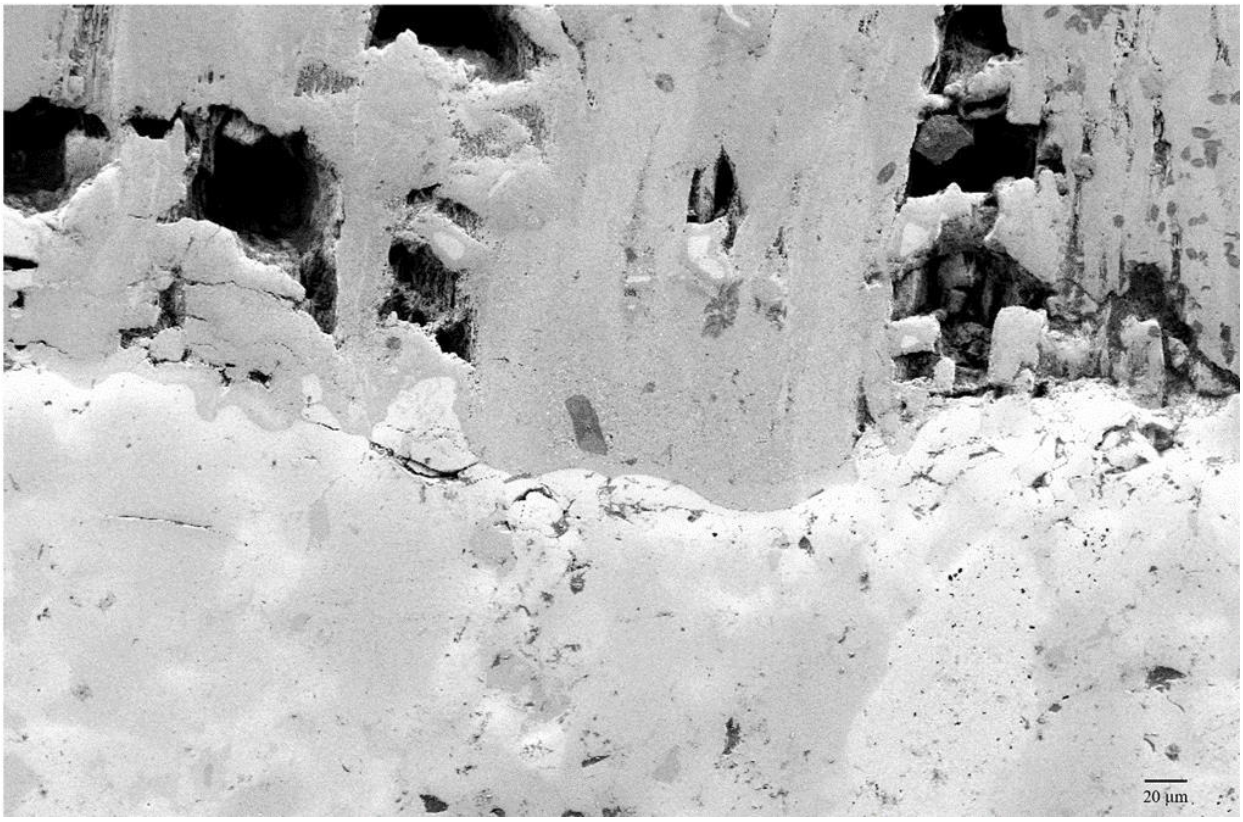

Figure 5: Bulk metal-oxide interface of the oxidized sample at 800^{o}C in the SE mode with large, prominent pores just above the interface.

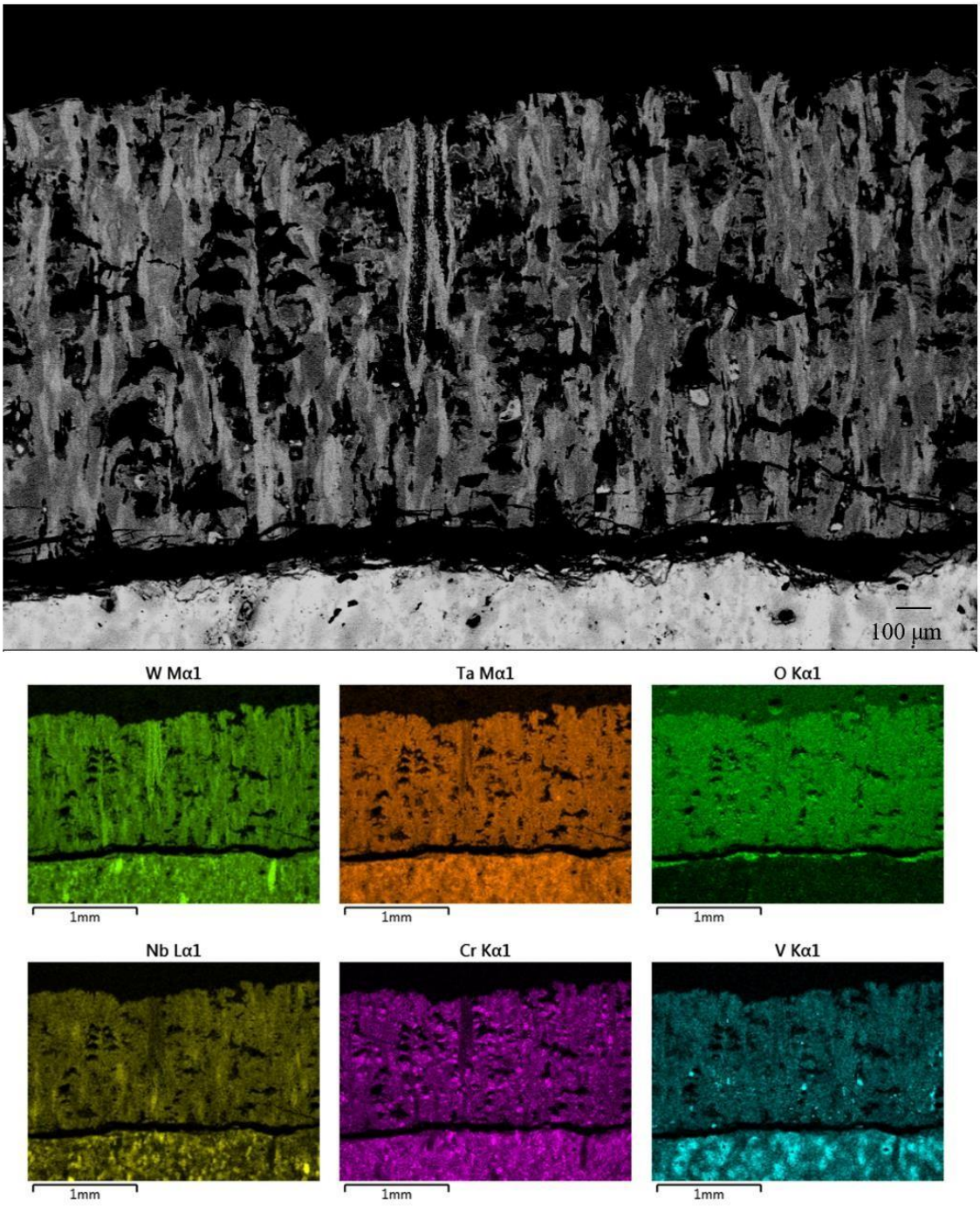

Figure 6: Bulk metal-oxide interface of the oxidized sample at 800°C in the BSE mode with EDS color mapping. Large, porous areas are visible throughout the oxide layer. Clusters of Cr are dispersed throughout the oxide layer. Strings of W with vertical upward growth in the layer are also dispersed throughout the oxide layer.

Figure 7: Bulk metal-oxide interface of the oxidized sample at 800ºC in the BSE mode indicating the thickness of the oxide layer.

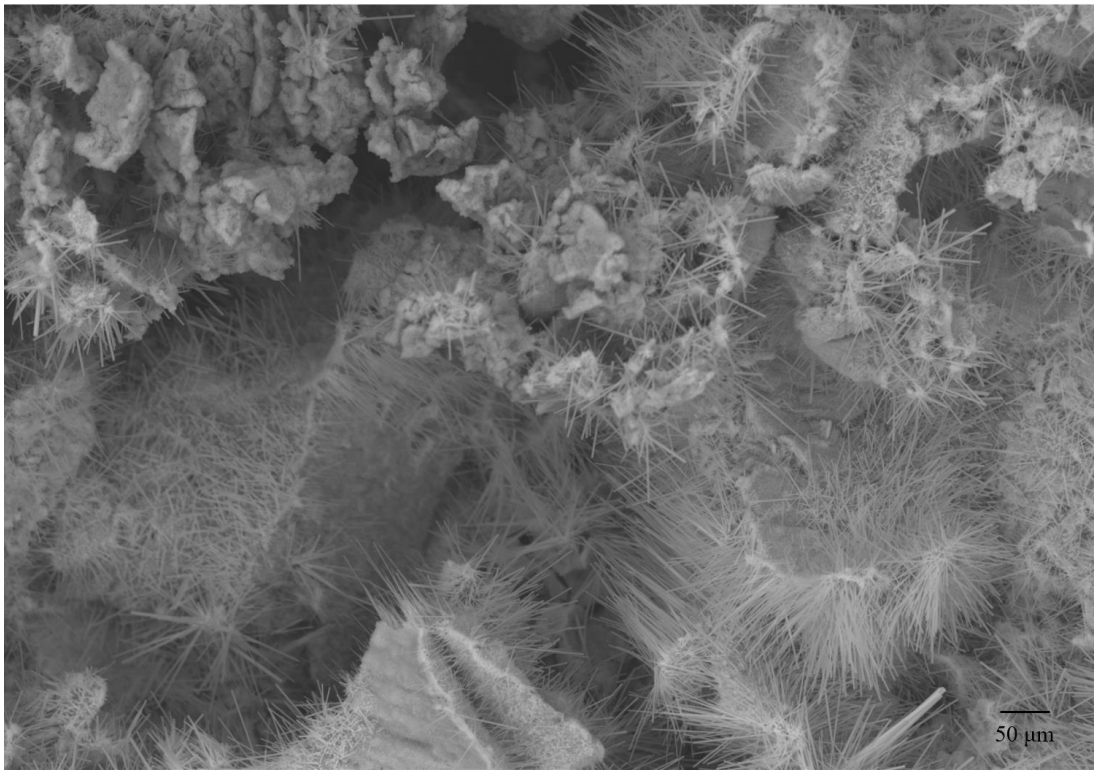

Figure 8: Surface of the oxide layer at 700°C in the BSE mode. The two main oxides are visible, the granular Cr-Ta oxide and the whisker-like W oxide.

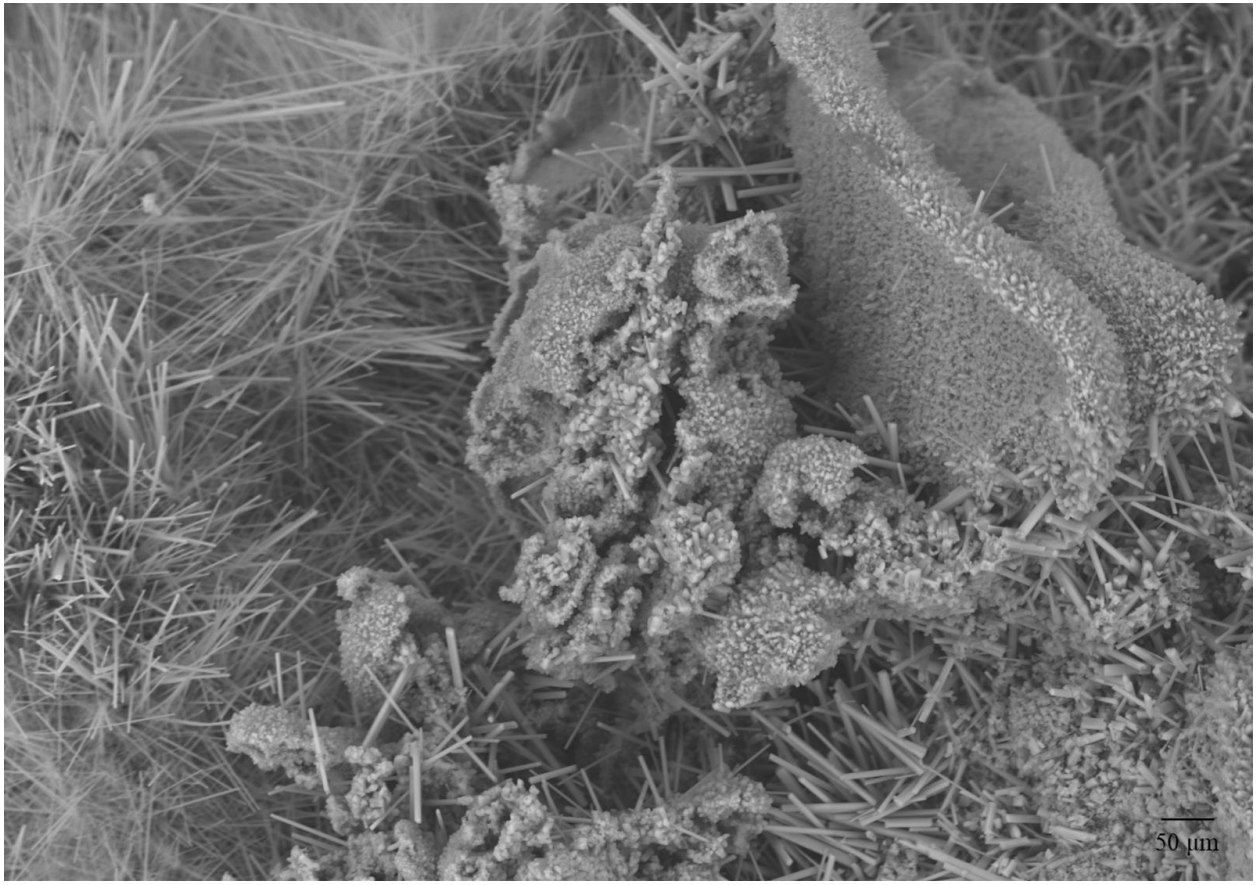

Figure 9: Surface of the oxide layer of the 800°C sample in the BSE mode. The granules of the Cr-Ta oxide have become more defined, while the W oxide has become more needle-like and is more prominent.

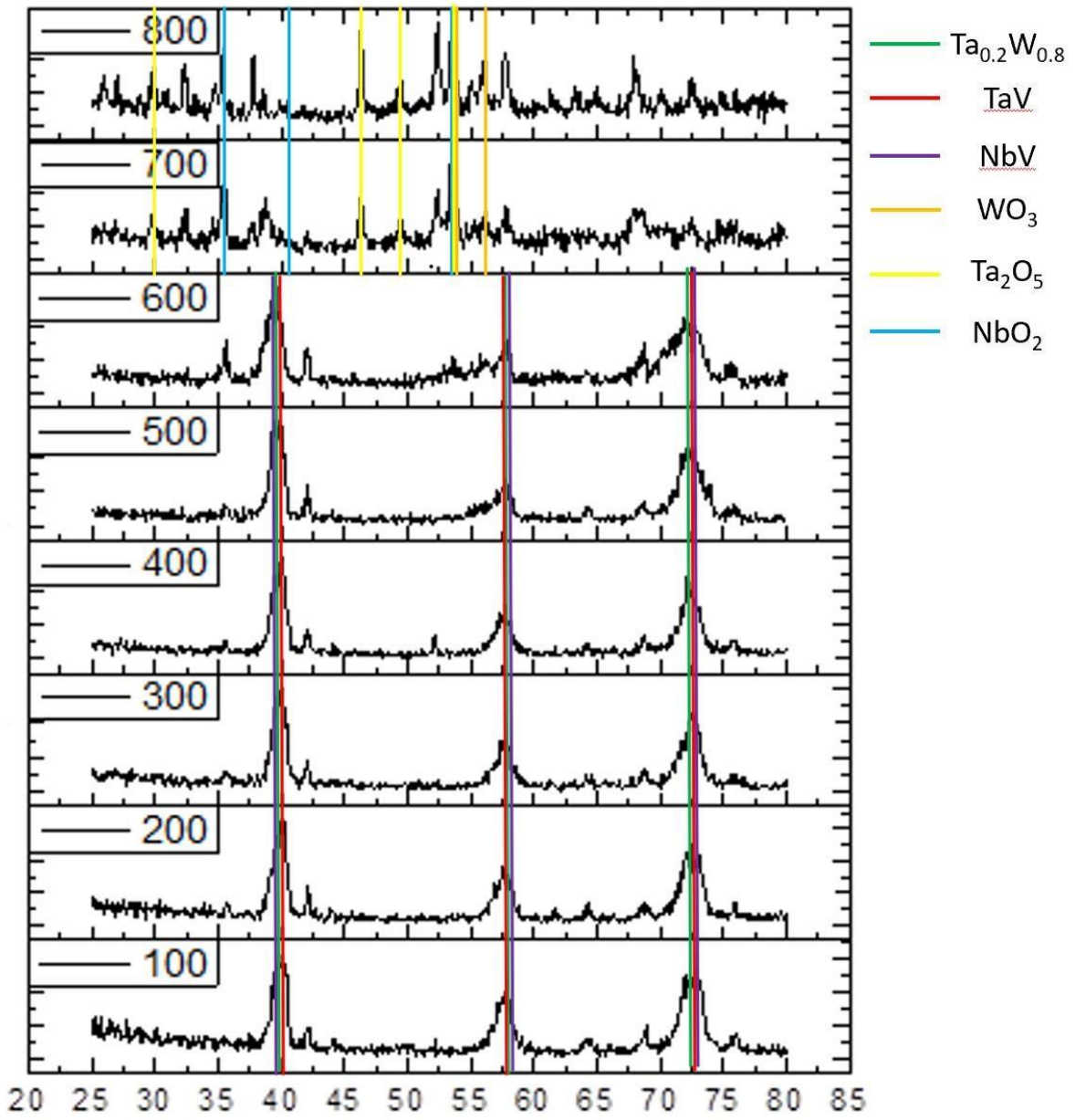

Figure 10: In-situ x-ray diffraction data of the HEAs.

Declaration

Declaration of interests

☒ The authors declare that they have no known competing financial interests or personal relationships that could have appeared to influence the work reported in this paper.

☐The authors declare the following financial interests/personal relationships which may be considered as potential competing interests: